Deficient RPE mitochondrial energetics leads to subretinal fibrosis in age-related neovascular macular degeneration

Check for updates

Xiang Ma[1,2,7], Wenjing Wu[1,3,7], Miwa Hara[1], Junwen Zhou[4], Carolina Panzarin[1,5], Christopher M. Schafer[2], Courtney T. Griffin [1,2], Jiyang Cai[6], Jian-Xing Ma [1,6] ✉ & Yusuke Takahashi [1,6] ✉

Subretinal fibrosis permanently impairs the vision of patients with neovascular age-related macular degeneration. Despite emerging evidence revealing the association between disturbed metabolism in retinal pigment epithelium (RPE) and subretinal fibrosis, the underlying mechanism remains unclear. In the present study, single-cell RNA sequencing revealed, prior to subretinal fibrosis, genes in mitochondrial fatty acid oxidation are downregulated in the RPE lacking very low-density lipoprotein receptor (VLDLR), especially the rate-limiting enzyme carnitine palmitoyltransferase 1A (CPT1A). We found that overexpression of CPT1A in the RPE of $Vldlr^{-/-}$ mice suppresses epithelial-to-mesenchymal transition and fibrosis. Mechanistically, TGFβ₂ induces fibrosis by activating a Warburg-like effect, i.e. increased glycolysis and decreased mitochondrial respiration through ERK-dependent CPT1A degradation. Moreover, VLDLR blocks the formation of the TGFβ receptor I/II complex by interacting with unglycosylated TGFβ receptor II. In conclusion, VLDLR suppresses fibrosis by attenuating TGFβ₂-induced metabolic reprogramming, and CPT1A is a potential target for treating subretinal fibrosis.

Age-related macular degeneration (AMD) is the leading cause of visual impairment in industrialized countries and profoundly impacts the physical and mental well-being of the elderly[1]. Ten to 15% of AMD patients develop neovascular AMD (nAMD), characterized by choroidal neovascularization (CNV)[2]. CNV and its complications, such as hemorrhage and fibrovascular scarring, cause irreversible blindness and account for more than 90% of visual symptoms[2]. Although anti-vascular endothelial growth factor (VEGF) therapy effectively ameliorates pathological angiogenesis in most nAMD patients, subretinal fibrosis, which is responsible for severe and permanent vision loss, remains untreatable. Moreover, recent studies have reported an association between anti-VEGF therapy and the increased risk of subretinal fibrosis[3,4]. Thus, it is urgent to advance our knowledge regarding subretinal fibrosis and its pathogenic mechanisms to develop alternative therapeutic options.

Dysfunction and degeneration of retinal pigment epithelial (RPE) cells are recognized as the core pathogenesis of AMD[5]. Among different types of CNV, those that damage the RPE layer are most likely to cause subretinal fibrosis[6]. In healthy conditions, a single RPE cell interacts with 20-30 photoreceptor cells and is responsible for phagocytosis of the photoreceptor outer segments, visual cycle, and nourishment of fragile neurons in the outer retina[7]. In nAMD, CNV penetrates the RPE monolayer, and exudation from leaky vessels generates an inflammatory environment in the subretinal region. This environment elicits an epithelial-mesenchymal transition (EMT) in disturbed RPE cells, leading to the loss of epithelial markers and gain of mesenchymal features, such as the production of extracellular matrix (ECM) and migration[8]. A recent study revealed that α-smooth muscle actin (α-SMA)-positive RPE cells are present in fibrous membranes associated with CNV in nAMD patients[9]. Moreover, healthy RPE cells have an enriched mitochondrial population and predominantly rely on mitochondrial metabolism (β-oxidation, oxidative phosphorylation, and TCA cycle) to produce adenosine triphosphate (ATP)[10]. In primary RPE cells from AMD patients, mitochondrial function is suppressed, and glycolysis is used as the primary energy source, which is a paradigm known as the Warburg effect[10]. However, the association between the metabolic reprogramming in RPE cells and subretinal fibrogenesis in AMD remains uncertain.

Very low-density lipoprotein receptor (VLDLR) was originally recognized as a member of the lipoprotein receptor family that mediates

[1]Department of Biochemistry, Wake Forest University School of Medicine, Winston-Salem, NC, USA. [2]Cardiovascular Biology Research Program, Oklahoma Medical Research Foundation, Oklahoma City, OK, USA. [3]Dean A. McGee Eye Institute, University of Oklahoma Health Sciences Center, Oklahoma City, OK, USA. [4]Health Economics Research Centre, Nuffield Department of Population Health, University of Oxford, Oxford, UK. [5]Laboratory of Metabolic Disorders, School of Applied Sciences, University of Campinas-UNICAMP, Limeira, Brazil. [6]Department of Physiology, University of Oklahoma Health Sciences Center, Oklahoma City, OK, USA. [7]These authors contributed equally: Xiang Ma, Wenjing Wu. ✉e-mail: jianma@wakehealth.edu; ytakahas@wakehealth.edu

Fig. 1 | Characterization of subretinal neovascularization and fibrosis in *Vldlr*^{−/−} mice. A 3D reconstruction of representative confocal images of isolectin-stained neovascularization of 1-month-old *Vldlr*^{−/−} and WT mice (Deep: deep retinal vascular layer). The scale bars in whole mount, inset, and 3D were 1000, 200, 10 μm, respectively. **B** Hematoxylin and eosin staining on the retinal sections of *Vldlr*^{−/−} and WT mice. The white arrow indicates a CNV lesion. Scale bar: 50 μm. **C** Representative immunostaining of α-SMA and fibronectin in an ocular cryosection of 3-month-old WT and *Vldlr*^{−/−} mice. The nuclei were counterstained with DAPI. Scale bar: 50 μm. Quantification of α-SMA-positive areas (**D**) and fibronectin-positive areas (**E**) in (**C**) (*n* = 6). **F** Representative Western blotting of α-SMA, CTGF, and fibronectin from eyecups of 3-month-old WT and *Vldlr*^{−/−} mice. Quantification of α-SMA (**G**), CTGF (**H**), and fibronectin (**I**) in (**F**) (*n* = 6). GCL ganglion cell layer, INL inner nuclear layer, ONL outer nuclear layer; RPE, retinal pigment epithelium. Data are presented as mean ± SD. *P < 0.05, **P < 0.01, ***P < 0.001.
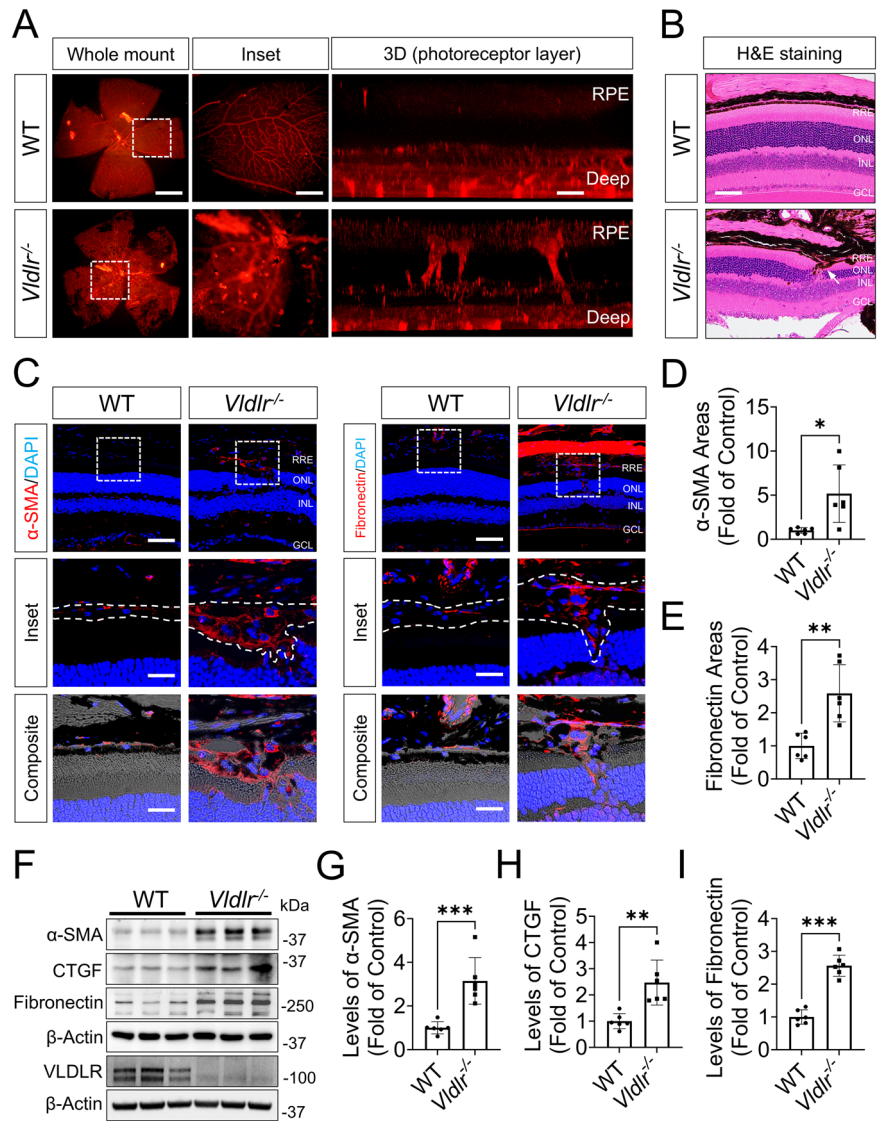
lipid uptake and metabolism in extra-hepatic tissues[11]. A genetic linkage study showed that VLDLR gene variants are associated with the risk of AMD[12]. *Vldlr*^{−/−} mice manifest multiple nAMD-like phenotypes, including spontaneous subretinal NV, vascular leakage, inflammation, and progressive decline of electroretinography (ERG) responses[13,14]. In addition, *Vldlr*^{−/−} mice have been established as a mouse model of subretinal fibrosis and nAMD pathologies[15,16]. Interestingly, RPE cells display regional heterogeneity based on their proximity to CNV lesions and non-CNV lesion areas. To better understand the underlying molecular mechanisms behind this cellular heterogeneity, single-cell RNA sequencing (scRNA-seq) was performed to compare the transcriptomic profiles of RPE cells from age-matched wildtype (WT) and *Vldlr*^{−/−} mice. Genes identified in this scRNA-seq dataset were validated using functional assays. The adeno-associated virus-mediated intervention was performed to explore the underlying mechanism of subretinal fibrosis in *Vldlr*^{−/−} mice. Collectively, the findings of this study identify a novel and pathogenic mechanism for the development of subretinal fibrosis in a nAMD model.

Results

Characterization of subretinal neovascularization and fibrosis in *Vldlr*^{−/−} mice

Two separate vascular networks support the nutrition and oxygenation of the neural retina. The inner retina is supported by retinal vasculature, whereas the outer retina is supported by choroidal vessels[17]. In *Vldlr*^{−/−} mice,

we found that retinal neovascularization penetrated the normally avascular photoreceptor layer and intact RPE layer, connecting the retinal and choroidal vascular networks and causing RPE detachment and melanocyte migration towards the photoreceptor layer (Fig. 1A, B, and Supplementary Fig. 1B). Knockout of VLDLR was confirmed by Western blotting and immunostaining (Fig. 1F and Supplementary Fig. 1A). Newly formed pathological vessels are leaky, and which triggers fibrosis in the eye[16]. Fundus fluorescein angiography (FFA), revealed an increase of fluorescein leakage in 1-month-old *Vldlr*^{−/−} mice compared to the age-matched WT mice (Supplementary Fig. 1C), and optical coherence tomography (OCT) detected multiple neovascular lesions with increased reflectivity in the subretinal region of *Vldlr*^{−/−} mice (Supplementary Fig. 1D). Immunostaining showed that fibrosis markers, including α-SMA (Fig. 1C, D), fibronectin (Fig. 1C, E), vimentin (Supplementary Fig. 1E, F), and collagen I (Supplementary Fig. 1E, G), were markedly increased at the CNV lesions and surrounding pigmented tissues of 3-month-old *Vldlr*^{−/−} mice. These changes indicate that disturbed RPE cells substantially contribute to fibrosis in CNV regions. In agreement with these data, Western blot analysis showed a robust increase of fibrosis markers, including α-SMA, connective tissue growth factor (CTGF), and fibronectin (Fig. 1F–I), in the eyecups of 3-month-old *Vldlr*^{−/−} mice compared to age-matched WT mice. Taken together, these results suggest that *Vldlr*^{−/−} mice serve as a good model for studying subretinal fibrosis, and RPE cells are major contributors to fibrogenesis in the eye.
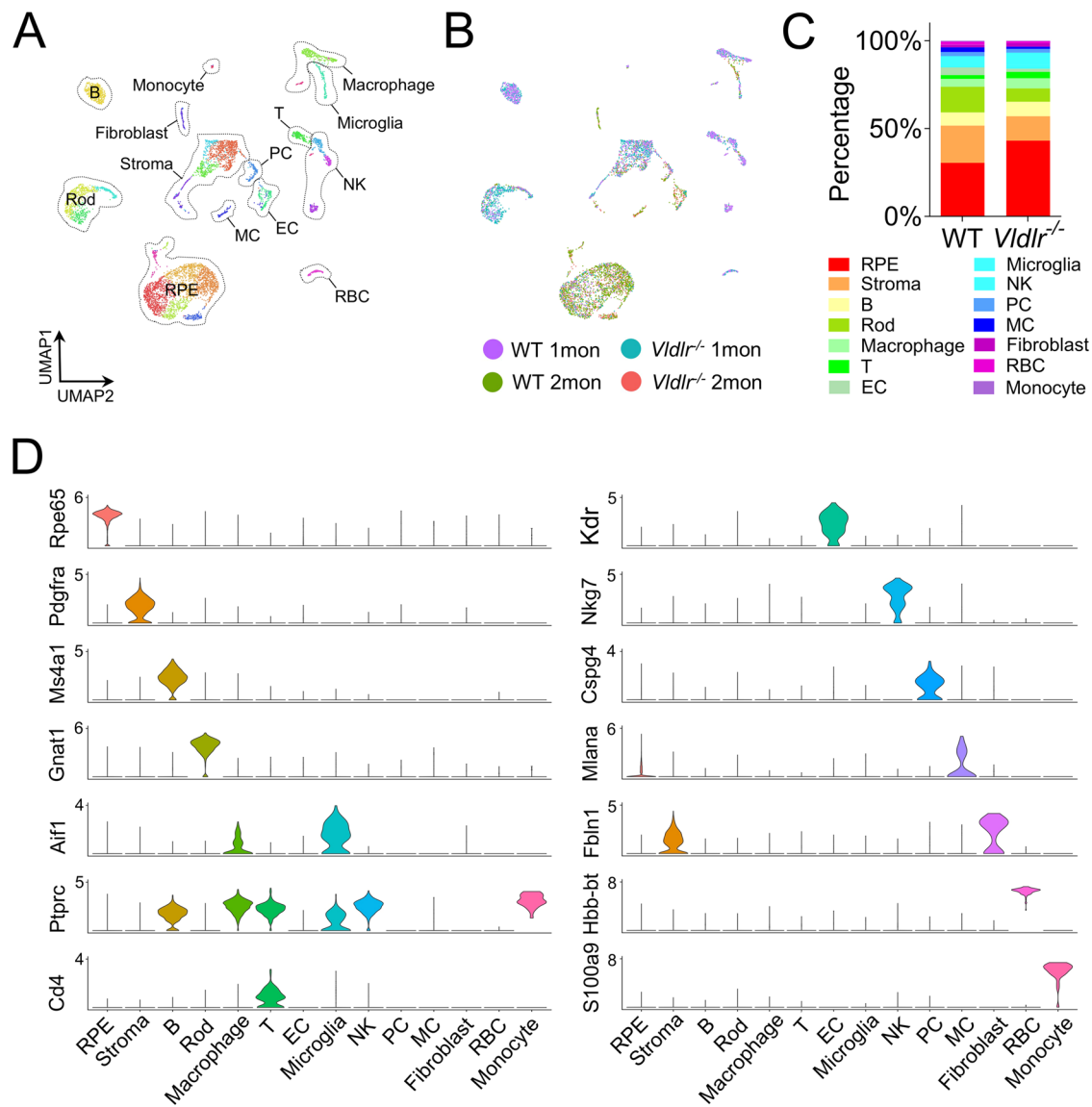
Fig. 2 | Cell clusters of scRNA-seq analysis from RPE-choroid tissues of _Vldlr_⁻/⁻ and WT mice. A A UMAP plot showing 14 different cell types identified in RPE-choroid tissues. EC, Endothelial cell; NK, natural killer cell; PC pericyte, MC melanocyte, RBC red blood cell, RPE retinal pigmented epithelium. **B** A UMAP plot showing the sample sources of WT and _Vldlr_⁻/⁻ mice at the age of 1 month and 2 months. **C** Percentage of different cell types between genotypes. **D** Violin plots showing the gene expression of known cell markers across different cell types.

scRNA-seq profile of RPE-choroid tissues from _Vldlr_⁻/⁻ mice

Single-cell transcriptomic analysis was performed on RPE-choroid tissues of WT and _Vldlr_⁻/⁻ mice at the ages of 1 and 2 months. Using a Seurat R package, a total of 7943 cells passed quality control and were grouped into 27 clusters, which were annotated into 14 different cell types (Fig. 2A). The differentially expressed genes in each cluster were listed in Supplementary Table 1. Among them, 4236 cells (53.3%) and 3,707 cells (46.7%) originated from WT and _Vldlr_⁻/⁻ RPE-choroid tissues, respectively. The distribution of each cluster in the WT and _Vldlr_⁻/⁻ groups was depicted in Fig. 2B, and the percentage of each cell type between genotypes was shown in Fig. 2C. The gene expression of known cell markers in eyecups was shown in violin plots in Fig. 2D and UMAP plots in Supplementary Fig. 2.

Mitochondria-related metabolism is downregulated in RPE cells of _Vldlr_⁻/⁻ mice

A total of 196 transcripts was significantly downregulated in the _Vldlr_⁻/⁻ RPE compared to WT RPE, which were used for Gene Ontology (GO) analysis. Among the most affected biological processes were aerobic respiration (GO:0009060, 17 counts; $p.adjust = 1.60 \times 10^{-11}$), cellular

respiration (GO:0045333, 18 counts, $p.adjust = 5.18 \times 10^{-11}$), energy derivation by oxidation of organic compounds (GO:0015980, 20 counts, $p.adjust = 7.17 \times 10^{-11}$), aerobic electron transport chain (GO:0019646, 10 counts, $p.adjust = 1.93 \times 10^{-9}$), generation of precursor metabolites and energy (GO:0006091, 21 counts; $p.adjust = 1.93 \times 10^{-9}$), oxidative phosphorylation (GO:0006119, 13 counts, $p.adjust = 3.38 \times 10^{-9}$), mitochondrial ATP synthesis coupled electron transport (GO:0042775, 10 counts, $p.adjust = 1.18 \times 10^{-8}$), and ATP synthesis coupled electron transport (GO:0042773, 10 counts, $p.adjust = 1.38 \times 10^{-8}$) (Fig. 3A and supplementary Table 2). GO analysis was supported by the Gene Set Enrichment Analysis (GSEA), in which genes involved in oxidative phosphorylation (normalized enrichment score, NES = −1.72, $p.adjust = 0.0028$), mitochondrial ATP synthesis coupled electron transport (NES = −1.69, $p.adjust = 0.0062$), and fatty acid β-oxidation (NES = −1.47, $p.adjust = 0.041$) featured as prominent downregulated biological pathways in _Vldlr_⁻/⁻ RPE compared to WT RPE (Fig. 3B).

We then focused on individual genes that were downregulated in _Vldlr_⁻/⁻ RPE which would be predicted to influence metabolic processes (Fig. 3C, D). These included known regulators of fatty acid β-oxidation
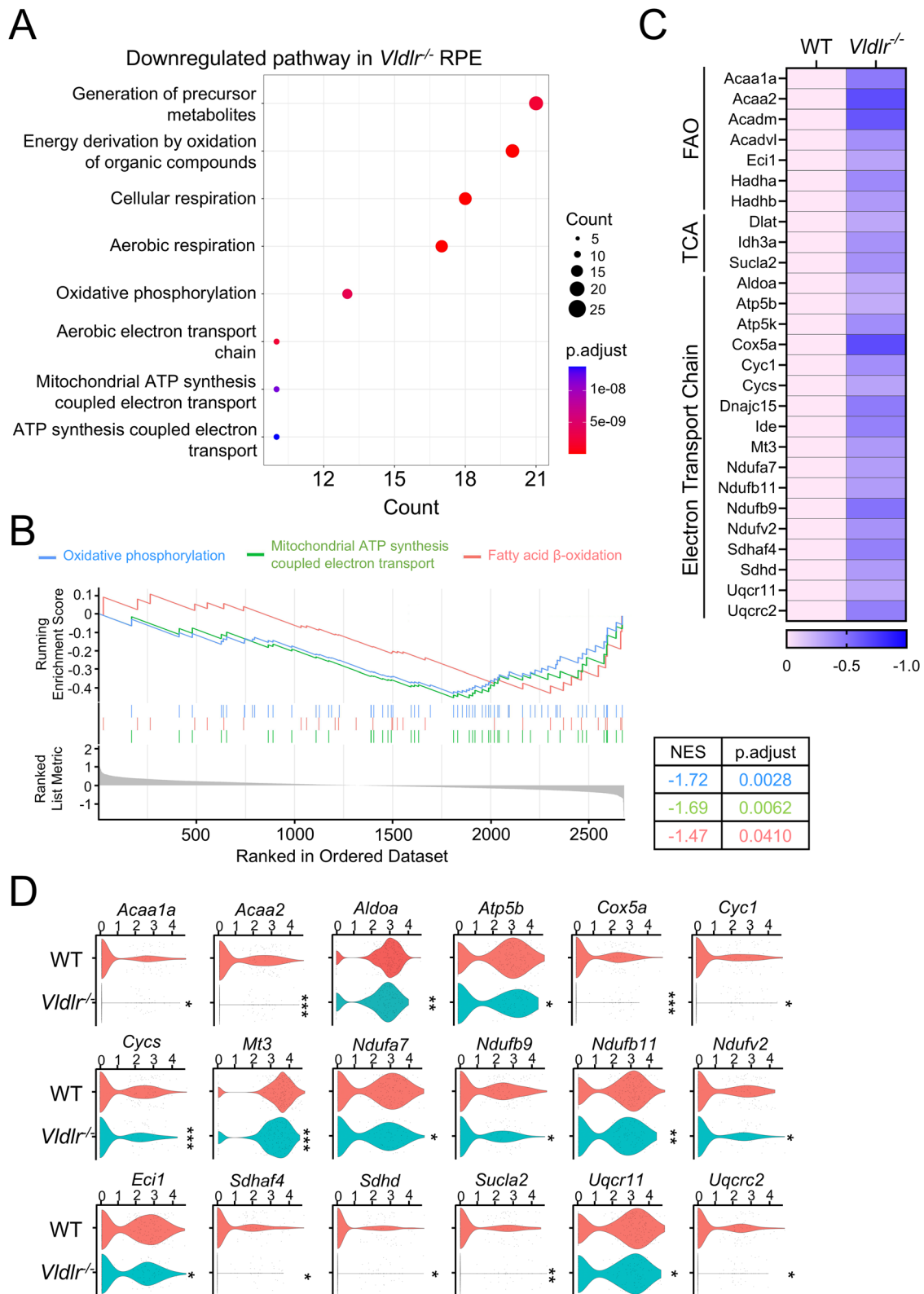
Fig. 3 | Transcriptional profiling of RPE cells from *Vldlr*⁻/⁻ and WT mice.
A Dotplot of top 8 downregulated biological processes in *Vldlr*⁻/⁻ RPE compared to WT RPE. Gene ontology (GO) enrichment analysis was performed based on 196 differentially expressed genes. The size of the dot indicates the number of downregulated genes. The color of the dot indicates statistical significance. **B** Prominently changed metabolic pathways were identified by Gene Set Enrichment Analysis (GSEA). NES: normalized enrichment score. **C** A heatmap of mitochondrial metabolism-related downregulated genes in *Vldlr*⁻/⁻ RPE compared to WT RPE. **D** Violin plots of mitochondrial metabolism-related genes downregulated in *Vldlr*⁻/⁻ RPE compared to WT RPE. * Adjusted *P* Value < 0.05, ** Adjusted *P* Value < 0.01, *** Adjusted *P* Value < 0.001.

(Acaa1a, Acaa2, Acadm, Acadvl, Eci1, Hadha, Hadhb), citric acid cycle function (Dlat, Idh3a, Sucla2), and electron transport chain activity (Aldoa, Atp5b, Atp5k, Cox5a, Cyc1, Cycs, Dnajc15, Ide, Mt3, Ndufa7, Ndufb11, Ndufb9, Ndufv2, Sdhaf4, Sdhd, Uqcr11, Uqcrc2). Taken together, these results suggest that mitochondria-related metabolism is downregulated in $Vldlr^{-/-}$ RPE.

Mitochondrial metabolism is functionally deficient in $Vldlr^{-/-}$ RPE cells

To verify that the observed downregulation of genes related to mitochondrial metabolism leads to a functional deficiency, a mitochondrial stress test was performed to measure oxygen consumption rate (OCR) in primary RPE cells. $Vldlr^{-/-}$ RPE cells had significantly lower basal OCR, maximal OCR, and spare capacity compared to WT RPE cells (Fig. 4A, B). Similarly, in a fatty acid β-oxidation (FAO) assay using a Seahorse analyzer, primary $Vldlr^{-/-}$ RPE cells demonstrated significantly lower basal OCR and maximal OCR relative to WT RPE cells (Fig. 4C, D), suggesting that RPE cells without VLDLR had less capacity for fatty acid utilization as an energy source.

To understand the fibrotic phenotype in $Vldlr^{-/-}$ retinas better, we focused on TGFβ, which is a master regulator of fibrosis[18] that is overactivated in $Vldlr^{-/-}$ retinas[16]. First, we examined the effect of TGFβ on mitochondrial metabolism in primary RPE cells. TGFβ$_2$ treatment decreased maximal OCR and spare respiratory capacity compared to vehicle control in human RPE cells (Fig. 4E–H). TGFβ$_2$ also suppressed FAO (basal OCR, maximal OCR, and spare capacity) in human RPE cells (Fig. 4I–L). Our previous work has demonstrated that VLDLR suppresses a synergistic effect of TGFβ and canonical Wnt signaling during fibrogenesis[15]. We now report that overexpression of VLDLR suppressed TGFβ$_2$-induced OCR downregulation (Fig. 4E–L). Moreover, overexpression of VLDLR suppressed TGFβ$_2$-induced profibrotic marker expression in human RPE cells, including α-SMA, CTGF, and fibronectin (Fig. 4M, N). Therefore, we found that the anti-fibrotic effect of VLDLR was associated with its impact on metabolic reprogramming.

A recent study showed that TGFβ may induce a Warburg-like effect to boost fibrosis in renal cells[19]. We therefore explored whether this also occurred in RPE cells. Indeed, we found that TGFβ$_2$ induced ATP production from glycolysis and suppressed ATP production from mitochondrial metabolism (Supplementary Fig. 3). To determine if such a transition to glycolysis leads to fibrogenesis, we examined whether an inhibitor of glycolysis, 2-deoxyglucose (2-DG), affected TGFβ-induced fibrosis. 2-DG inhibited TGFβ$_2$-induced expression of α-SMA, CTGF, and fibronectin in human RPE cells (Fig. 4O, P), indicating that VLDLR suppressed TGFβ-induced fibrosis through blocking the TGFβ-mediated downregulation of oxidative phosphorylation and upregulation of glycolysis.

Carnitine palmitoyltransferase 1A (CPT1A) is downregulated in $Vldlr^{-/-}$ mice and nAMD patients

Among the metabolic genes significantly downregulated in $Vldlr^{-/-}$ RPE, we identified downregulation of CPT1A from our scRNA-seq dataset, an enzyme that catalyzes a critical rate-limiting step during β-oxidation (Fig. 5A). CPT1A is located on the outer mitochondrial membrane and converts fatty acyl-CoA and carnitine into fatty acylcarnitine, a key step in the transport of fatty acids into the mitochondrial matrix[20]. A recent study suggests that CPT1A plays an anti-fibrotic role in kidney fibrosis[19]. $Cpt1a$ downregulation was confirmed by traditional qPCR using mRNA isolated from primary $Vldlr^{-/-}$ and WT RPE (Fig. 5B). Furthermore, protein levels of CPT1A were significantly decreased in the RPE from $Vldlr^{-/-}$ mice compared to the RPE from WT mice (Fig. 5C, D).

Based on the importance of CPT1A in fatty acid oxidation and the downregulation of CPT1A in $Vldlr^{-/-}$ RPE, we decided to pursue the role of CPT1A in subretinal fibrosis and mitochondrial function. Importantly, we also found a significant downregulation of VLDLR and CPT1A, and upregulation of α-SMA in human retinal sections from nAMD patients compared to age-matched non-AMD controls, particularly in the RPE layer (Fig. 5E–H). Donor demographics were tabulated in Fig. 5F. Furthermore, we observed an association between the

downregulation of CPT1A and the upregulation of fibrosis markers in the RPE of nAMD patients (Fig. 5H).

Overexpression of CPT1A suppresses subretinal fibrosis

We then measured the effect of CPT1A overexpression on metabolism and fibrosis in human primary RPE cells. Overexpression of CPT1A using an adenovirus expression system attenuated the TGFβ$_2$-induced downregulation of maximal OCR and spare capacity in the FAO assay (Fig. 6A–D). Overexpression of CPT1A similarly suppressed the TGFβ$_2$-induced upregulation of glycolysis and glycolytic capacity (Fig. 6E–H). Furthermore, overexpression of CPT1A significantly reduced TGFβ$_2$-induced upregulation of α-SMA, CTGF, and fibronectin protein expression in human RPE cells (Fig. 6I, J), indicating that overexpression of CPT1A attenuates TGFβ-induced metabolic reprogramming, leading to the protective effects against TGFβ-induced EMT and fibrosis in RPE cells.

Next, we investigated the effect of CPT1A overexpression on fibrosis in $Vldlr^{-/-}$ mice. AAV containing $Best1$ promoter-driven human CPT1A overexpression (AAV-$Best1$-CPT1A) was used to target the RPE layer specifically. Subretinal injection of AAV-$Best1$-CPT1A was performed in $Vldlr^{-/-}$ mice at the age of P14, and retinal function and fibrosis were measured at the age of 2 months. CPT1A overexpression by subretinal injection of AAV-$Best1$-CPT1A was validated using both immunostaining and Western blot analysis and comparison with contralateral eyes injected with AAV-EGFP (control) (Fig. 6K, L). Compared to controls, CPT1A overexpression led to decreased fibrotic areas of collagen I, α-SMA, and CTGF in eyecup flatmounts (Fig. 6K, Supplementary Fig. 4A, B). Moreover, as shown by Western blot, CPT1A overexpression led to a decrease of α-SMA, CTGF, and fibronectin (Fig. 6L and Supplementary Fig. 4C). Finally, eyes with CPT1A overexpression showed significantly higher ERG response compared to control eyes in $Vldlr^{-/-}$ mice, including scotopic a wave, scoptoic b wave, and photopic b wave (Supplementary Fig. 4D–H). Taken together, these results suggest that overexpression of CPT1A suppresses subretinal fibrosis and prevents retinal functional decline in $Vldlr^{-/-}$ mice.

TGFβ downregulates CPT1A and promotes fibrosis in an ERK-dependent manner

We next investigated how TGFβ regulated CPT1A expression. TGFβ$_2$ treatment induced a time-dependent downregulation of CPT1A in primary human RPE cells (Fig. 7A, B). Downregulation of CPT1A preceded the upregulation of fibrosis markers, further suggesting its causal effect on fibrosis (Fig. 7A, B). Recent studies have shown that MAPK/ERK is required for TGFβ-mediated biological processes, including metabolic reprogramming, EMT, and fibrosis[21]. We therefore evaluated the effect of ERK in TGFβ-mediated CPT1A downregulation. Knockdown (KD) of ERK1/2 by siRNA attenuated TGFβ$_2$-induced downregulation of CPT1A and upregulation of fibrosis markers (CTGF and fibronectin) (Fig. 7C, D). These results suggest that TGFβ regulates CPT1A and fibrosis in an ERK-dependent manner. Finally, CHX protein degradation assay showed that TGFβ$_2$ promoted CPT1A degradation, which blocked by MG132, suggesting that TGFβ$_2$ induces CPT1A downregulation by promoting its proteasome-mediated degradation (Fig. 7E–G).

The anti-fibrotic effect of CPT1A depends on its lipid-transport function

Etomoxir (Eto) suppresses the CPT1A-mediated formation of fatty acylcarnitine and blocks the entrance of fatty acid into the mitochondrial matrix[20]. We applied Eto to test if the anti-fibrotic effect of CPT1A was dependent on its lipid-transport role. Eto had a mild effect on the upregulation of CPT1A, which might be the compensatory effect (Supplementary Fig. 5A, B). Then, we found that Eto blocked the CPT1A overexpression-mediated anti-fibrotic effect (Supplementary Fig. 5C–E), suggesting that the anti-fibrotic effect of CPT1A is dependent on its lipid-transport function.

In addition, the knockdown of CPT1A had no significant effect on fibrosis markers in the absence of TGFβ$_2$. However, knockdown of CPT1A
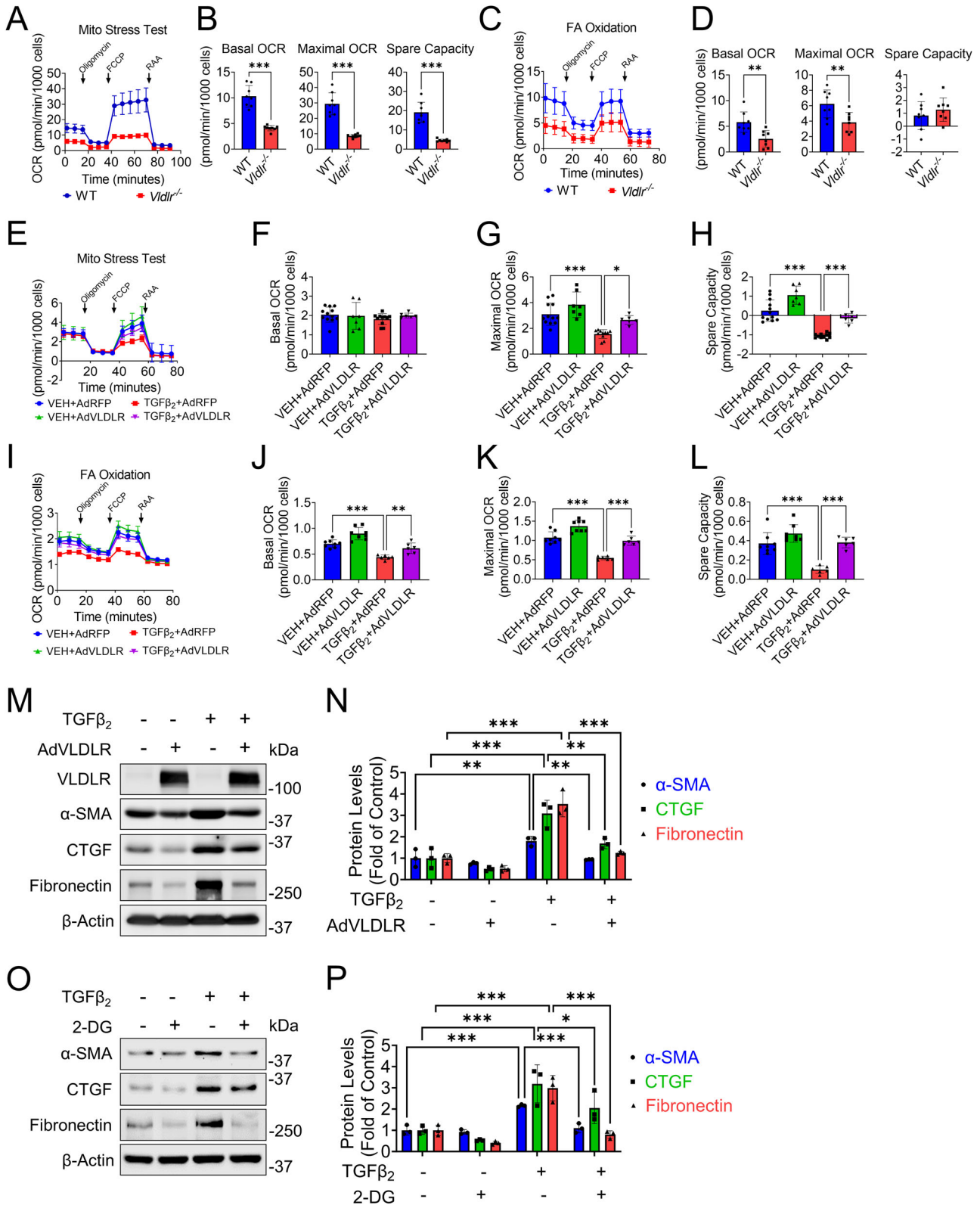
suppressed fibrosis marker expression in the presence of TGFβ₂, suggesting that CPT1A-mediated mitochondrial metabolism is an important energy source for physiological homeostasis (Supplementary Fig. 5F–I). Although the Warburg-like effect triggers profibrotic change, mitochondrial energetic pathways supports fibrogenesis by producing ATP and TCA intermediates[22].
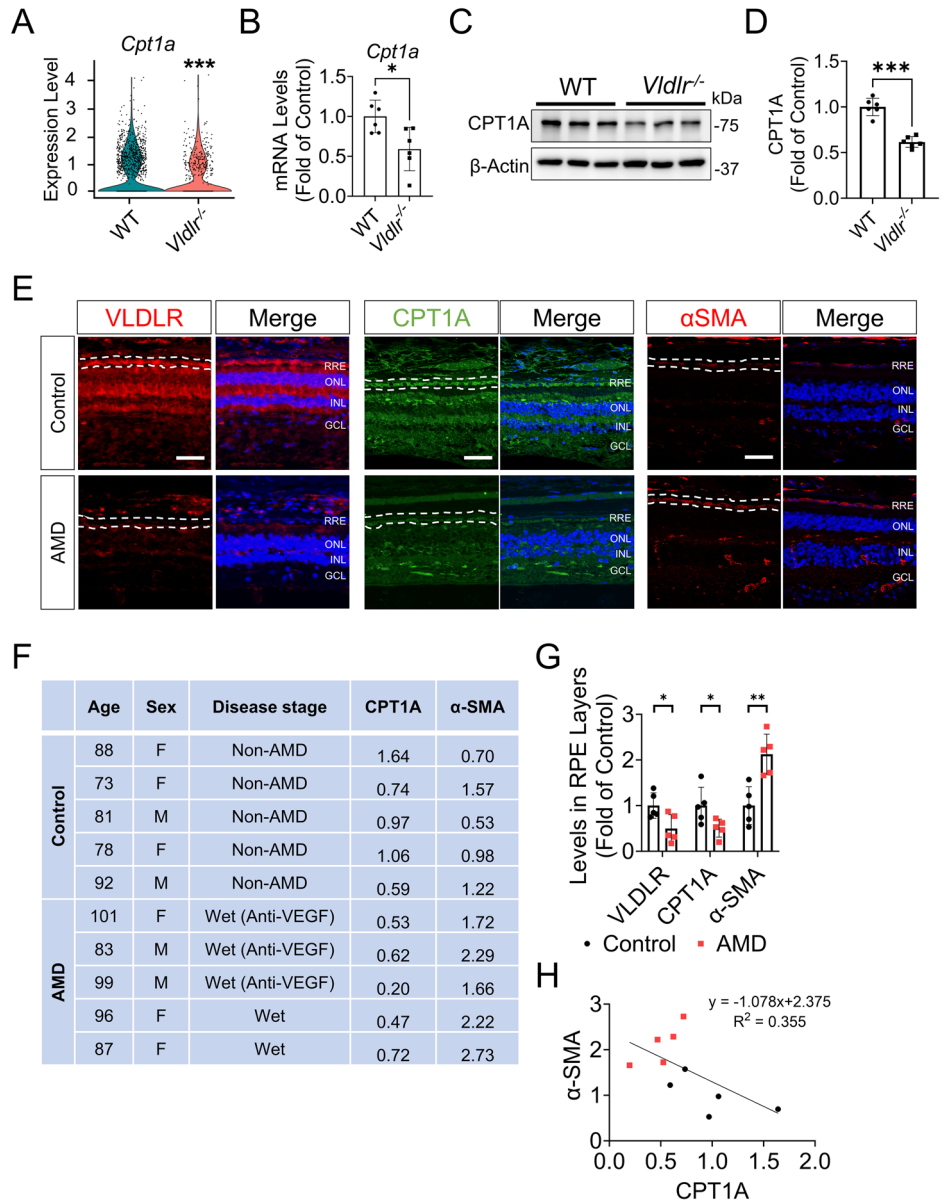
VLDLR confers an anti-fibrotic effect through interaction with TGFβ receptor II

A previous study showed that TGFβ receptor II is upregulated in *Vldlr⁻/⁻* mice, contributing to the overactivated TGFβ signaling and subsequent fibrosis in the subretinal region[16]. We therefore investigated if VLDLR confers an anti-TGFβ signaling effect at the receptor level using vectors

Fig. 4 | Functions of mitochondrial metabolism in RPE of *Vldlr*⁻/⁻ mice and in fibrotic stress. A Mitochondrial stress test in primary RPE cells from WT and *Vldlr*⁻/⁻ mice. **B** Basal oxygen consumption rate (OCR), maximal OCR, and spare capacity were compared between genotypes (*n* = 8). **C** Fatty acid (FA) oxidation (FAO) was measured in primary RPE cells from WT and *Vldlr*⁻/⁻ mice. Palmitate (170 μM) was used as the only energy substrate for oxidative phosphorylation. **D** Basal OCR, maximal OCR, and spare capacity were compared between groups (*n* = 8). Metabolism of human primary RPE cells treated with AdVLDLR and TGFβ₂. Human primary RPE cells were infected with AdVLDLR or AdRFP as control (MOI = 50) for 24 h. Then, cells were treated with 5 ng/ml TGFβ₂ or vehicle (VEH) for 24 h. Cells were then used for seahorse assays (**E–L**) or Western blot analysis (**M–P**). **E** Mitochondrial stress test in human primary RPE cells treated with

indicated conditions. During the test, RPE cells were incubated in a basic Seahorse XF DMEM medium supplemented with 1 mM pyruvate, 2 mM glutamine, and 10 mM glucose. Basal OCR (**F**), maximal OCR (**G**), and spare capacity (**H**) were compared between groups (*n* = 6–12). **I** FA oxidation was measured in human primary RPE cells treated with indicated conditions. Basal OCR (**J**), maximal OCR (**K**), and spare capacity (**L**) were compared between groups (*n* = 6–8). **M** Representative Western blots of fibrosis markers in human primary RPE cells treated with indicated conditions. **N** Levels of α-SMA, CTGF, and fibronectin in (**M**) were quantified (*n* = 3). **O** Representative Western blots of human RPE cells treated with TGFβ₂ with or without 2 g/L 2-deoxy-D-glucose (2-DG, the derivative of glucose). **P** Levels of α-SMA, CTGF, and fibronectin in (**O**) were quantified (*n* = 3). Data are presented as mean ± SD. *P < 0.05, **P < 0.01, ***P < 0.001.

Fig. 5 | Downregulation of CPT1A is correlated with fibrosis in *Vldlr*⁻/⁻ mice and nAMD patients. A Violin plot of *Cpt1a* in RPE clusters from WT and *Vldlr*⁻/⁻ mice measured by scRNA-seq analysis. The Y-axis indicates the normalized counts of *Cpt1a* transcript. *** Adjusted *P* Value < 0.001. **B** mRNA levels of *Cpt1a* in WT RPE and *Vldlr*⁻/⁻ RPE measured by qPCR (*n* = 6). **C** Representative Western blotting of CPT1A in RPE isolated from 2-month-old WT and *Vldlr*⁻/⁻ mice. **D** Quantification of protein levels of CPT1A in (**C**) (*n* = 6). **E** Representative immunostaining of VLDLR, CPT1A, and α-SMA in the subretinal areas of nAMD patients and controls. **F** Human AMD donors demographics. The age, sex, disease stage, CPT1A intensity, and α-SMA intensity of nAMD patients and non-AMD controls. **G** Quantification of VLDLR, CPT1A, and α-SMA in the RPE layer of AMD patients and controls in (**E**) (*n* = 5 for non-AMD controls, *n* = 5 for nAMD patients). VLDLR and CPT1A intensities were significantly lower in AMD patients compared to control (both *P* < 0.05), while α-SMA was significantly higher (*P* < 0.01). **H** The correlation between levels of CPT1A and α-SMA in the subretinal areas of nAMD patients and controls (*n* = 5 for non-AMD controls, *n* = 5 for nAMD patients). Data are presented as mean ± SD. *P < 0.05, **P < 0.01, ***P < 0.001.

	Age	Sex	Disease stage	CPT1A	α-SMA
Control	88	F	Non-AMD	1.64	0.70
	73	F	Non-AMD	0.74	1.57
	81	M	Non-AMD	0.97	0.53
	78	F	Non-AMD	1.06	0.98
	92	M	Non-AMD	0.59	1.22
AMD	101	F	Wet (Anti-VEGF)	0.53	1.72
	83	M	Wet (Anti-VEGF)	0.62	2.29
	99	M	Wet (Anti-VEGF)	0.20	1.66
	96	F	Wet	0.47	2.22
	87	F	Wet	0.72	2.73

overexpressing Myc-tagged VLDLR, Flag-tagged TGFβ receptor II, and His-tagged TGFβ receptor I. PNPLA2/ATGL was used as a non-binding negative control. Immunoprecipitation of Myc-tagged VLDLR coprecipitated the Flag-tagged TGFβ receptor II (Fig. 8A). Similarly, Myc-tagged VLDLR was coprecipitated by an anti-Flag pull down of TGFβ receptor II (Fig. 8B), suggesting that VLDLR is physically associated with TGFβ receptors. More interestingly, we found that VLDLR is exclusively bound

with unglycosylated TGF-β receptor II. Unglycosylated TGF-β receptor II is more likely to recruit and form the heterotetramer with TGF-β receptor I, contributing to downstream activation of TGFβ signaling[23]. This result indicates that VLDLR is a highly efficient and selective anti-fibrotic element.

Our previous work demonstrated that VLDLR confers an anti-canonical Wnt signaling effect via binding with the Wnt co-receptor LRP6[24]. LRP6 was shown to interact with TGFβ receptors[25]. In addition, synergy was
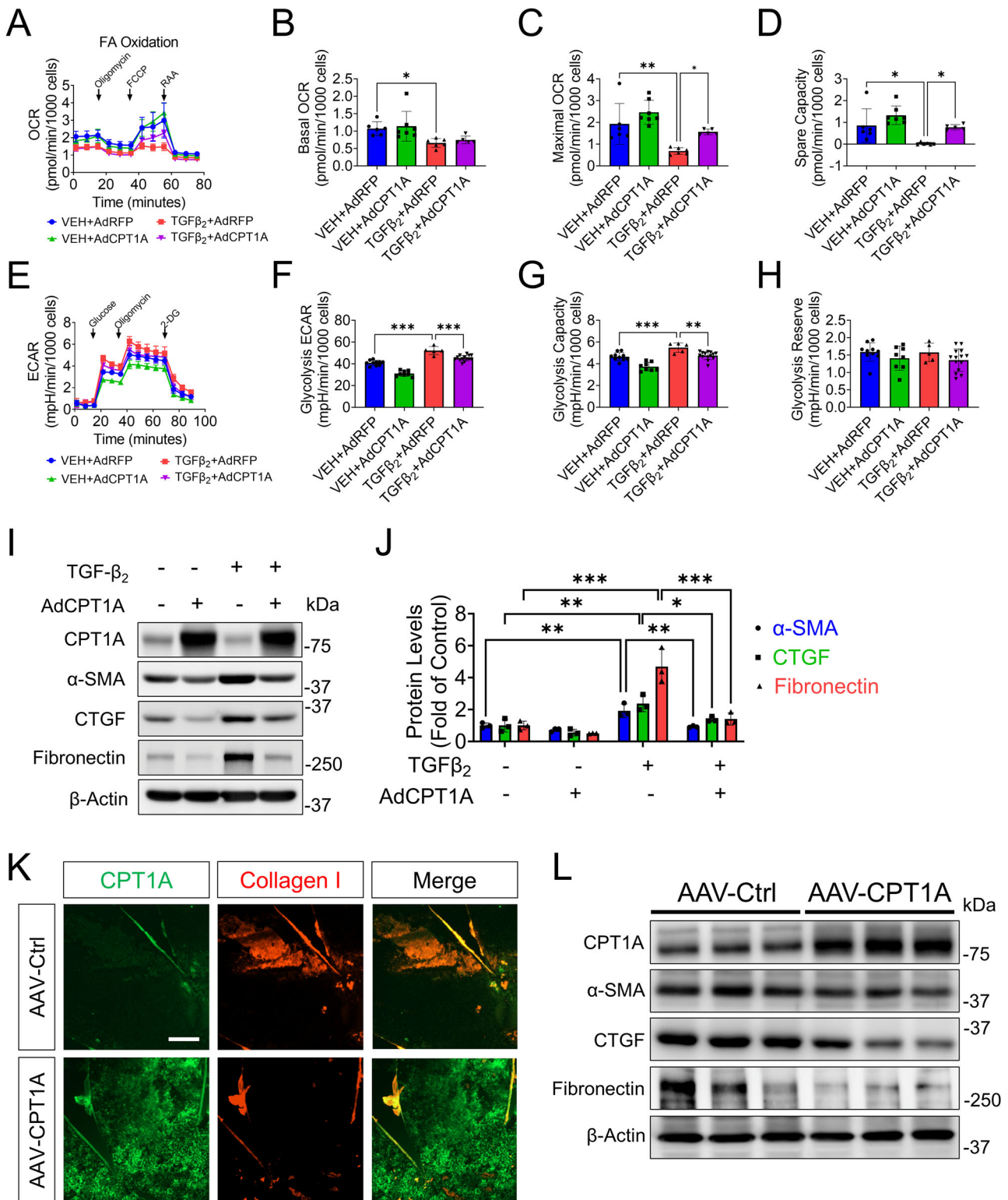
Fig. 6 | Overexpression of CPT1A ameliorates mitochondrial dysfunction and fibrosis in human RPE cells. A–J Human primary RPE cells were used for mitochondrial metabolism and fibrosis analysis. Cells were transduced with AdCPT1A or AdRFP as control (MOI = 50) for 24 h. Then, cells were treated with 5 ng/ml TGFβ₂ or vehicle (VEH) for 24 h and were used for Seahorse assay (**A–H**) or Western blot analysis (**I, J**). **A** FAO was measured in human primary RPE cells treated with indicated conditions. Basal OCR (**B**), maximal OCR (**C**), and spare capacity (D) were compared between groups (*n* = 5–7). **E** Glycolysis stress test was measured in human primary RPE cells treated with indicated conditions. Glycolysis (**F**), glycolytic capacity (**G**), and glycolytic reserve (**H**) were compared between groups (*n* = 5–14).

I Representative western blots of fibrosis markers in human primary RPE cells treated with indicated conditions. **J** Levels α-SMA, CTGF, and fibronectin in (I) were quantified (*n* = 3). Data are presented as mean ± SD. *P < 0.05, **P < 0.01, ***P < 0.001. **K, L** Human CPT1A was overexpressed in *Vldlr⁻/⁻* mice to investigate the anti-fibrotic effect of CPT1A. One microliter of 2 × 10¹³ gene copy (GC)/ml of AAV-*Best1-CPT1A* was subretinally injected into *Vldlr⁻/⁻* pups at the age of P14. The contralateral eye was injected with AAV-*GFP* at the same titer. **K:** Representative immunostaining of CPT1A (green) and collagen I (red) in the flatmounted eyecup at 6 weeks post injection. Scale bar: 100 μm. **L** Representative western blot analysis of CPT1A, α-SMA, CTGF, and fibronectin.
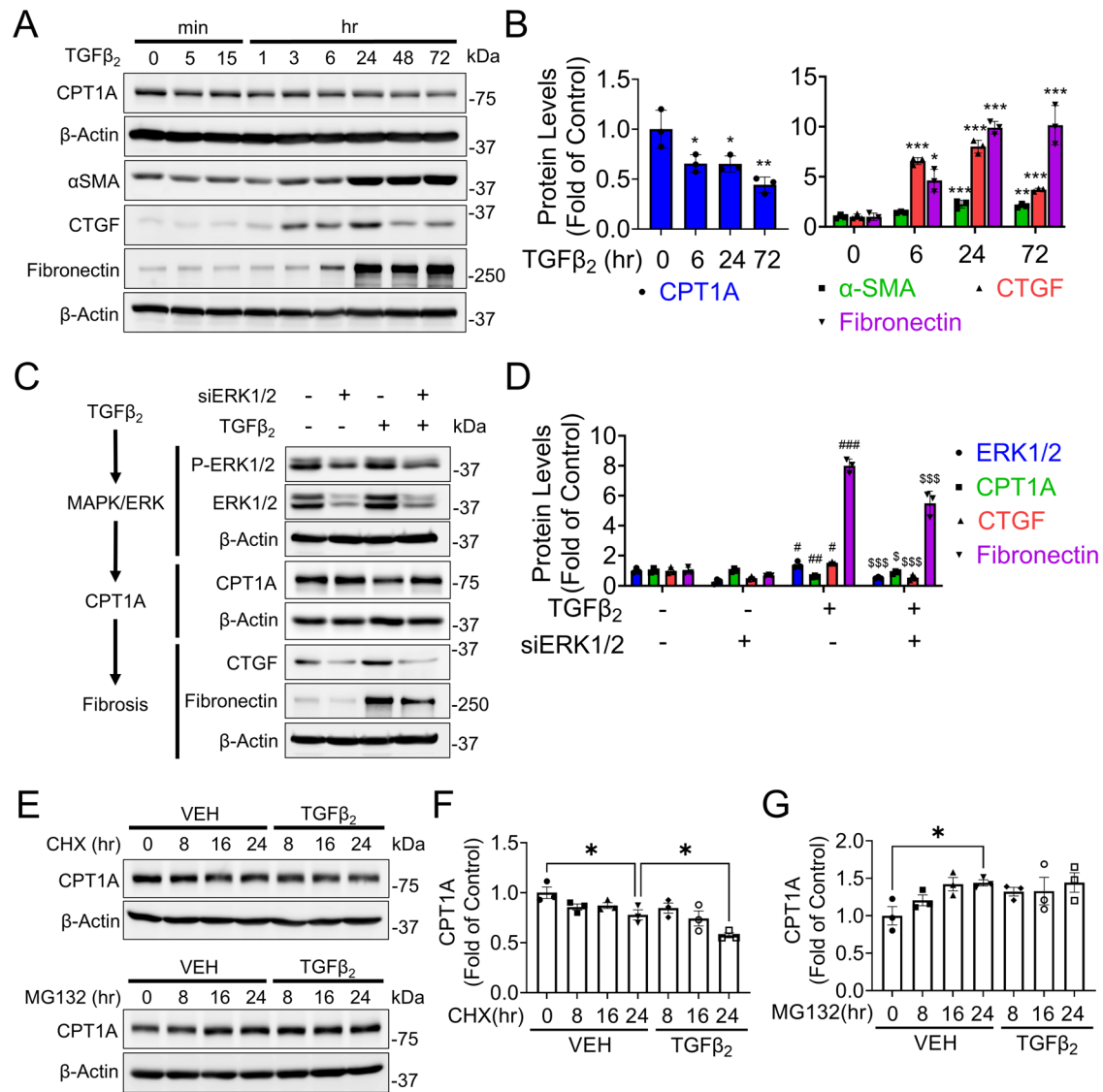
Fig. 7 | TGFβ signaling regulates CPT1A in an ERK-dependent manner.
A Representative images of western blot analyses in human primary RPE cells treated with 5 ng/ml TGFβ₂ for the indicated duration. **B** Levels of CPT1A, α-SMA, CTGF, and fibronectin in (**A**) were quantified (*n* = 3). One-way ANOVA analysis was used to compare each time point with the control (0 h). **C** Representative Western blots of human primary RPE cells treated with siRNA for ERK1 and ERK2 (ERK1/2), or scrambled siRNA as control for 48 h, followed by 5 ng/ml TGFβ₂ for 24 h. **D** Levels of ERK1/2, CPT1A, fibronectin, and CTGF in (**C**) were quantified (*n* = 3). One-way ANOVA analysis was used to compare each group to third group

with TGFβ₂ and scramble siRNA. Symbol # indicates statistical significance between the first group and the third group. Symbol $ indicates statistical significance between the fourth group and the third group. **E** Representative Western blots of human primary RPE cells treated with 50 μg/ml cycloheximide (CHX, protein synthesis inhibitor) or 5 μM MG132 (proteinase inhibitor) without or with 5 ng/ml TGFβ₂ for indicated durations. **F**, **G** Levels of CPT1A in (**E**) were quantified (*n* = 3). Data are presented as mean ± SD. *$P < 0.05$, **$P < 0.01$, ***$P < 0.001$, #$P < 0.05$, ##$P < 0.01$, ###$P < 0.001$, \$$P < 0.05$, \$\$$P < 0.01$, \$\$\$$P < 0.001$.

demonstrated between Wnt and TGFβ signaling in promoting fibrosis[15]. Since we found that VLDLR suppressed TGFβ₂-induced phosphorylation of Smad2/3 (P-Smad2/3) independent of Wnt coreceptors (Supplementary Fig. 6B–E), we decided to determine if VLDLR interacts with TGFβ receptors via Wnt coreceptors. We performed head-to-head comparison of binding between VLDLR and TGFβ receptor in WT ARPE-19 cells, *LRP5* KO ARPE-19 cells, and *LRP6* KO ARPE-19 cells. ARPE-19 cells with *LRP5* KO or *LRP6* KO were generated using CRISPR/Cas9 techniques and validated (Supplementary Fig. 6A)[15,26]. We found that when Myc-tag was pulled down, TGFβ receptor II was coprecipitated regardless of the presence of LRP5 or LRP6 (Fig. 8C), suggesting that VLDLR interacts with the TGFβ receptor independently of Wnt coreceptors.

TGFβ ligands are known to promote the heterotetramer formation of TGFβ receptors[27], which was confirmed in human RPE cells. In the presence

of TGFβ₂, the pulldown of Flag-tag led to higher co-immunoprecipitation of TGFβ receptor I (Fig. 8D). Overexpression of VLDLR suppressed TGFβ₂-induced heterotetramerization of TGFβ receptor I and II (Fig. 8D). These results suggest that VLDLR suppresses TGFβ signaling by blocking the heterotetramer formation of TGFβ receptors.

The anti-fibrotic effect of VLDLR is independent of its well-known function in lipid uptake
Last, we studied the effect of the soluble ectodomain of VLDLR (sVLDLR) on TGFβ-mediated metabolic reprogramming and fibrogenesis. We found that overexpression of sVLDLR (without the VLDLR transmembrane domain) suppressed TGFβ₂-mediated upregulation of glycolysis (glycolysis ECAR, glycolytic capacity, and glycolytic reserve) (Supplementary Fig. 7A–D). In addition, overexpression of sVLDLR suppressed
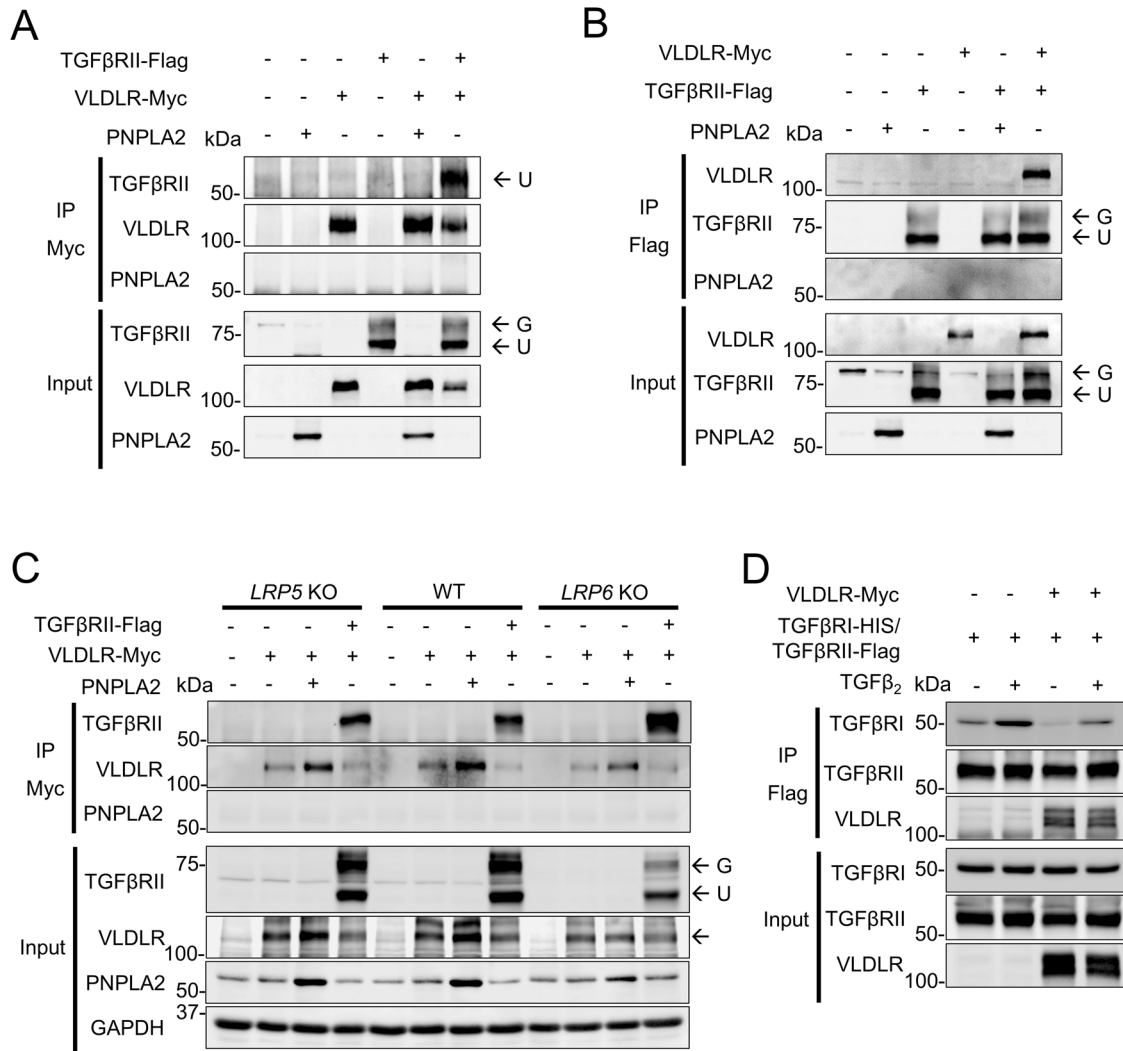
Fig. 8 | VLDLR blocks the formation of the heterotetramers of TGFβ receptors by interacting with unglycosylated TGFβ receptor II, which is independent of Wnt coreceptors. Human primary RPE cells (**A**, **B**, **D**), WT ARPE-19 cells, and ARPE-19 cells with *LRP5* KO or *LRP6* KO (**C**) were used for co-immunoprecipitation (co-IP). Cells were transfected with plasmids to overexpress indicated proteins for 48 h, and then cells were harvested with co-IP buffer for pulldown and Western blot analysis. **A** Interaction between VLDLR and TGFβ receptor II (TGFβRII) by Myc-tag pull-down. Membrane protein PNPLA2 was used as the negative control. G: glycosylated TGFβRII, U: unglycosylated TGFβRII. **B** Interaction between VLDLR and TGFβ receptor II (TGFβRII) by Flag-tag pulldown. Membrane protein PNPLA2 was used as the negative control. G: glycosylated TGFβRII, U: unglycosylated TGFβRII. **C** Interaction between VLDLR and TGFβ receptor II (TGFβRII) tested in WT, *LRP5*, or *LRP6* KO cells. G: glycosylated TGFβRII, U: unglycosylated TGFβRII, the arrow indicates the VLDLR band. **D** VLDLR effect on the interaction between TGFβRI and TGFβRII. Forty-eight hours after transfection, cells were treated with 5 ng/ml TGFβ₂ or vehicle for 15 min and used for co-immunoprecipitation.

TGFβ₂-mediated upregulation of fibrosis markers (α-SMA, CTGF, and fibronectin) (Supplementary Fig. 7E, F). These results suggest that VLDLR plays an anti-fibrotic effect that is independent of its lipid-uptake function.

Discussion

In this study, scRNA-seq was used to identify cellular and molecular regulators of subretinal fibrosis. By analyzing the transcriptomic profiles of RPE cells, we found that RPE cells in a murine nAMD model displayed mesenchymal phenotypes with upregulated fibrogenic pathways and downregulated pathways related to mitochondrial metabolism, especially lipid metabolism (Supplementary Fig. 8). TGFβ, the master fibrogenic factor, promoted fibrosis in RPE cells through metabolic reprogramming from mitochondria oxidation to glycolysis as the primary energy source. Mechanistically, we found that TGFβ₂ induced metabolic reprogramming via the regulation of CPT1A, the key enzyme facilitating the transport of fatty acid into the mitochondrial matrix. The downregulation of CPT1A was found to associate with fibrosis in human nAMD patients as well as the

nAMD animal model. The deficiency of CPT1A promoted fibrosis, while overexpression of CPT1A rescued the subretinal fibrosis both in vivo and in vitro. Furthermore, we found that TGFβ₂ mediated CPT1A down-regulation in an ERK-dependent manner. Collectively, these findings suggest that CPT1A downregulation in AMD plays an important role in metabolic reprogramming in the RPE, leading to fibrosis.

Although anti-VEGF therapy is highly effective in inhibiting pathological angiogenesis, subretinal fibrosis is untreatable. Fibrosis is commonly regarded as a wound-healing process that fails to terminate and resolve[28]. TGFβ is the key profibrotic mediator while it is also a multifunctional cytokine with other functions such as neurotrophic effects[29,30]. Therefore, identifying the signaling events that precede fibrosis may reveal novel therapeutic targets. In *Vldlr⁻/⁻* mice, subretinal neovascularization initiates from P12, and subretinal fibrosis presents from P60[16]. *Vldlr⁻/⁻* RPE cells gained mesenchymal phenotypes with the induction of multiple signaling pathways, including Wnt and TGFβ signaling, ECM organization, and collagen-activated signaling, suggesting EMT. Meanwhile, the major downregulated signaling pathways identified in *Vldlr⁻/⁻* RPE cells

were related to mitochondrial metabolism, including fatty acid β-oxidation, the TCA cycle, and oxidative phosphorylation. These results suggest that the metabolic reprogramming is associated with EMT and later fibrogenesis.

The RPE predominantly relies on mitochondria to generate ATP to meet energy demands[10]. Unlike other tissues, the fatty acid β-oxidation process is highly utilized since RPE cells have plenty of fatty acid supply from the daily phagocytosis of photoreceptor outer segments[10]. A recent study identified metabolic coupling between RPE and photoreceptors[31]. Since glucose from the choroid passes through the RPE layer to reach photoreceptors, photoreceptors then utilize the glucose for glycolysis to perform light-sensing functions and maintain photoreceptor homeostasis. Lactate, a metabolic byproduct of glycolysis, is then shipped back to the RPE for energy production via oxidative phosphorylation. Moreover, lactate can also suppress glycolysis in RPE cells. AMD disturbed this metabolic ecosystem between RPE cells and the retina by shifting RPE cells from utilizing mitochondrial metabolism to glycolysis[31]. However, the underlying mechanism that triggers this metabolic shift remains unclear.

In the present study, we provide evidence that TGFβ is one of the major players initiating metabolic reprogramming in RPE cells towards glycolysis. The results of our scRNA-seq analyses led us to discover the role of CPT1A in TGFβ2-induced metabolic reprogramming and subsequent fibrogenesis. The mRNA level of *Cpt1a* was downregulated in RPE clusters in *Vldlr*$^{-/-}$ mice compared to that in WT controls (Fig. 5), and RPE of patients with nAMD showed substantially lower CPT1A protein levels compared to non-AMD controls (Fig. 5). Moreover, this downregulation of CPT1A expression was associated with abnormal increases of fibrosis marker in ocular sections from AMD donors (Fig. 5). Overexpression of CPT1A in RPE cells attenuated fibrosis in subretinal regions of *Vldlr*$^{-/-}$ mice (Fig. 6). Deficient lipid metabolism can boost pathological angiogenesis in endothelial cells in the eyes[32]. Therefore, RPE-specific overexpression of CPT1A via AAV may have a long-term anti-fibrotic effect while avoiding the potentiation of angiogenesis in the eyes. In addition, recent studies have reported that MAPK/ERK signaling is essential for metabolic reprogramming in tumor cells[21]. In agreement with this, we found that disruption of MAPK/ERK signaling attenuated TGFβ-induced CPT1A downregulation and suppressed TGFβ-mediated fibrosis. These results suggest that TGFβ-mediated CPT1A downregulation is dependent on the ERK pathway.

VLDLR is a lipid receptor and mediates lipid uptake[33]. It has been shown that *Vldlr* KO results in FAO decline in photoreceptors and, consequently, retinal degeneration due to energetic crisis[33]. However, the *Vldlr* KO-induced decline of mitochondria oxidation is unlikely due to decreased lipid uptake to the RPE, since RPE has a sufficient supply of fatty acid from the phagocytosis of the photoreceptor outer segment. In support of this notion is our observation that sVLDLR, the soluble extracellular domain of VLDLR without the transmembrane and intracellular domains, can rescue the metabolic disturbance (Supplementary Fig. 7), i.e, switching from mitochondrial oxidation to glycolysis in the RPE of *Vldlr*$^{-/-}$ mice or in primary RPE cells stimulated by TGFβ.

Mechanistically, we found that VLDLR physically interacted with unglycosylated TGFβ receptor II, suppressing the formation of heterotetramer of TGFβ receptor I and II. This effect is independent of the Wnt coreceptors, LRP5 and LRP6. Upon the activation of TGFβ signaling, TGFβ binds with TGFβ receptor II, which then recruits and phosphorylates TGFβ receptor I, leading to the activation of downstream profibrotic signaling[27]. A recent study demonstrated that glycosylation of the TGFβ receptors is a crucial regulation of TGFβ signaling[23]. Unglycosylated TGFβ receptor II is more likely to form the heterotetramers with TGFβ receptor I, activating TGFβ signaling[23]. Previously, we demonstrated that VLDLR physically interacts with Wnt co-receptor LRP6[24]. LRP6 was shown to promote TGFβ signaling by binding and stabilizing the TGFβ receptors[25]. Thus, we tested if VLDLR interacts with the TGFβ receptors through LRP6 in the present study. By ablating *LRP5* or *LRP6* in RPE cells, we found that interaction between VLDLR and TGFβ receptors still occurred, suggesting the interaction of VLDLR with TGFβ receptors is independent of the Wnt co-

receptor LRP5 or LRP6. Moreover, we confirmed that overexpression of sVLDLR further suppressed TGFβ-induced p-Smad2/3 in either *LRP5* or *LRP6* KO cells, indicating that VLDLR plays an anti-TGFβ signaling role that is independent of Wnt coreceptors. In the end, we also demonstrated that VLDLR blocked TGFβ ligand-induced formation of the TGFβ receptor heterotetramer.

Future studies are warranted to explore RPE cell heterogeneity and its potential role in fibrosis. Spatiotemporal studies could be informative if these activated RPE cells are in the proximity of CNV lesions and how they interact with surrounding immune cells and endothelial cells. Further mechanical studies are needed to understand how the initial downregulation of FAO and electron transport chain pathways contributes to fibrosis in AMD. It may be explained by profibrotic factor-induced metabolic reprogramming from oxidative phosphorylation towards the glycolysis pathway. First, shifting towards the glycolysis in fibrosis could provide rapid ATP generation to promote EMT and ECM production[22,28,34]. Glycolysis is approximately 100 times faster than oxidative phosphorylation in ATP production[35]. Second, recent studies reported that the glycolytic byproducts serine and glycine are essential substrates for collagen synthesis[22]. Third, it is possible that glycolytic by-products may stabilize the phosphorylation of profibrotic Smad family members, such as Smad2/3. Future studies on glycolytic by-products in fibrosis may provide more insights. Last, this work demonstrated that VLDLR blocks TGFβ signaling at the TGFβ receptor level, and VLDLR restores TGFβ-induced dysfunction of mitochondrial lipid transport (CPT1A route). Recent studies showed the molecular mechanism through other routes that TGFβ signaling may suppress the TCA cycle metabolism through the reduction of the transcription factor PGC-1α[36]. TGFβ may downregulate OCR through the induction of mitochondrial fission[37]. Future studies are needed to investigate if VLDLR restores TGFβ-induced metabolic dysfunction through routes other than CPT1A.

In conclusion, we constructed the transcriptome landscape of RPE cells in the nAMD model and acquired key information regarding the association between dysregulated metabolic profiles and fibrogenesis in RPE cells. We found that CPT1A served as a key regulator of metabolic reprogramming and consequent RPE cell EMT in the nAMD. Moreover, TGFβ mediated CPT1A downregulation in an ERK-dependent manner. Our study identified a potential therapeutic target for subretinal fibrosis and may contribute to preventing or slowing down vision loss in millions of patients with nAMD.

Methods
Animals
Vldlr$^{-/-}$ mice and WT mice on the C57BL/6J background were obtained from Jackson Laboratory (Bar Harbor, ME). Mice were housed in a specific pathogen-free (SPF) environment at 25 °C under a 12/12 h light/dark cycle in the animal facility of the University of Oklahoma Health Sciences Center (OUHSC) and Wake Forest University School of Medicine (WFUSM). Mice were cared for in compliance with the guidelines of the Association for Research in Vision and Ophthalmology (ARVO) Statement for the Use of Animals in Ophthalmic and Visual Research, and all studies were conducted following the protocol approved by the Institutional Animal Care and Use Committees (IACUC) at OUHSC and WFUSM.

Subretinal injection
Subretinal injections were performed in P14 mice according to a previously published protocol with minor modifications[38]. Briefly, following pupil dilation with tropicamide ophthalmic solution, USP1% (Bausch Health, NJ USA), mice were anesthetized with 100 mg/kg ketamine hydrochloride and 10 mg/kg xylazine. Eyes were kept moist throughout the procedure by the application of lubricant eyedrops. A sclerotomy was performed at 1 mm posterior to the limbus with a 25 G sterilized needle. Using a Nanofil syringe, a 33 G blunt needle was introduced through the opening at a 60° angle to avoid touching the lens. Once at the retina, gentle pressure was applied to the needle to penetrate the retina and access the subretinal space. Controlled

delivery of 1 μl of AAV-CPT1A (2.0×10^{13} genome copies (GC)/ml) or control AAV-GFP was administered at 200 nl/s into the subretinal space using the commercially available UMP3 UltraMicroPump system Nanofil RPE-Kit (WPI, Sarasota, FL, USA). Post injection, mice were allowed to recover on a heating pad while erythromycin ophthalmic ointment 0.5% (Bausch Health, NJ, USA) was applied gently to the corneas to protect them from infection. In the same mouse, the contralateral eye was injected with control AAV. In addition, age-matched mice without injections were used as sham controls.

Adenovirus, adeno-associated virus, and plasmids
Adenovirus type 5 overexpressing human CPT1A (AdCPT1A) was purchased from SignaGen Laboratories (Rockville, MD). AdVLDLR (full-length) was prepared by the Gene Vector Core at the Baylor College of Medicine[39]. AdsVLDLR (soluble ectodomain of VLDLR) and AdRFP were generated in-house. Adeno-associated virus type 2 (AAV2) overexpressing bestrophin1 (BEST1) promoter-driven human CPT1A was generated through a contract service with VectorBuilder (Chicago, IL). As a negative control, AAV2-GFP was purchased from VectorBuilder.

The vector pCMV6 expressing human VLDLR with a Myc tag at the C-terminus was purchased from OriGene Technologies (Rockville, MD). pRK5 vector for human TGFβ receptor II with a Flag tag at the C-terminus was a gift from Rik Derynck (#31719, Addgene, Watertown, MA) and pCMV5 vector for human TGFβ receptor I with a HIS tag at the C-terminus was a gift from Joan Massague (#19161, Addgene). The expression vector for PNPLA2 was generated in-house[40].

Cell culture
Primary human RPE cells were purchased from Lonza (Basel, Switzerland) and cultured in DMEM containing 2% fetal bovine serum (FBS), 5 ng/ml hFGF, N1 supplement (1X), and 1% penicillin/streptomycin, as described[41]. ARPE-19, a cell line derived from human RPE cells, was purchased from ATCC (Manassas, VA, USA) and cultured in DMEM/F12 medium containing 10% FBS and 1% Penicillin/Streptomycin. ARPE-19 cell lines with *LRP5* KO or with *LRP6* KO were generated using CRISPR/Cas9 technology[15,26]. Primary cultures of mouse RPE cells were established as previously described[15,42,43]. Briefly, the eyeballs were enucleated from 4- to 6-week-old mice. Connective tissues were carefully removed from the eyeballs in a sterile environment, and RPE-choroid-sclera complexes (eyecups) were gently dissected from the eyeballs. The eyecups were incubated with HBSS buffer containing 0.25% trypsin at 37 °C for 30 min. The RPE sheets were then gently peeled from the eyecups, and the RPE cell suspension was neutralized by culture media containing 10% FBS. Primary mouse RPE cells were cultured in MEM α supplemented with 10% FBS, N1 supplement (1×), MEM non-essential amino acid (1×), 2 mM L-glutamine, and 1% penicillin/streptomycin. All cells were routinely cultured in a humidified atmosphere containing 5% CO_2 at 37 °C.

For the adenovirus transduction, RPE cells were infected with adenovirus at a multiplicity of infection (MOI) of 50 for 48 h. For siRNA-mediated knockdown, siRNA SMARTpools for human ERK1/2, CPT1A, and scramble control were purchased from Dharmacon (Lafayette, CO). SiRNA target sequences were listed in Supplementary Table 3. Lipofectamine 2000 (Invitrogen, Carlsbad, CA) was used to transfect siRNAs (50 nM) or plasmids into cells according to the manufacturer's instructions.

Single-cell preparation and sequencing
RPE-choroid tissues were harvested from WT and *Vldlr*$^{-/-}$ mice at the ages of 1 month and 2 months. The isolation of viable single cells from RPE-choroid tissue was performed according to a published protocol[44,45]. Briefly, the eyeballs were enucleated and kept in pre-chilled PBS. Extraocular muscles were cleaned from the eyeballs, and a circumferential incision around the limbus was performed to remove the anterior segments. The neural retina was then gently separated from the RPE. RPE-choroid tissues were gently scraped from the sclera and sequentially digested with collagenase A (6.25 mg/ml) and Dispase II (6.25 mg/ml) at 37 °C for 15 min

and then with Trypsin (0.25%) at 37 °C for 5 min. After neutralization in a buffer containing 10% FBS, the tissue suspension was filtered through a 40-μm strainer to generate a single cell suspension. Dead Cell Removal Kit (Miltenyi Biotec, San Jose, CA) was used to eliminate dead cells. A low-speed (200 g, 10 min) and large-volume (40 ml in 50 ml tube) wash was performed to remove the cellular debris. Finally, the dissociated RPE/choroid cells with viability higher than 90%, as measured by a trypan blue assay, were used for cDNA library construction.

Cell suspensions in PBS containing 0.5% BSA with a density of approximate 200 cells/μl were used on the 10x Genomics Chromium platform to generate barcoded single-cell gel bead-in-emulsion (GEMs), targeting ~ 5000 cells per library. Barcoded libraries were sequenced on an Illumina HiSeq4000 (Illumina, USA) at Wake Forest University Cancer Genomics Shared Resource (CGSR).

Single-cell analysis
Raw sequencing data were generated in .fastq files and converted to a single-cell expression matrix in the Cell Ranger pipeline (version 3.0, 10x Genomics, USA). Data analysis and visualization were performed using the Seurat package (version 4.0; https://satijalab.org/seurat/index.html) in R studio (version 4.2.1; https://cran.r-project.org/bin/windows/base/)[46]. Cells with detected genes between 100 and 10,000 and with less than 25% mitochondrial genes were kept. Genes that were expressed by more than 3 cells were kept. After the filter step, 7943 cells (WT: 4236 cells and *Vldlr*$^{-/-}$: 3707 cells) were used for downstream analysis. To eliminate batch variability, "FindIntegrationAnchors" function was used to integrate 4 datasets from WT and *Vldlr*$^{-/-}$ mice at ages of 1 month and 2 months.

Unsupervised clustering analysis was conducted using the Seurat R package[46]. After normalizing data using the "LogNormalize" method, principal component analysis (PCA) was performed to reduce dimensionality with the top 30 principal component (PC) calculated. Based on p values from "JackStrawPlot", FindClusters function with a resolution of 1.0 was used to identify 27 different clusters. Clusters were virtualized in Uniform Manifold Approximation and Projection (UMAP). Differentially expressed genes among clusters were listed using "FindAllMarkers" function and matched with known cell markers[44]. Markers across all clusters were shown in stacked violin plots and UMAP plots.

Gene Ontology (GO) enrichment analysis and Gene Set Enrichment Analysis (GSEA) were performed using the ClusterProfiler package (version 4.0)[47]. Significantly up- and downregulated genes of *Vldlr*$^{-/-}$ mice compared to WT mice were used for analyses. Biological pathways with the largest changes were virtualized using the dotplot function of ggplot2 package. Differential gene expression between clusters from different genotypes was analyzed using the "Findmarker" function in the Seurat package. The fold change of gene expression and adjusted *p* values were calculated with a Bonferroni correction.

Seahorse assay
Primary mouse RPE cells were cultured in the media mentioned above until confluence. Before treatment, cells were starved in culture media containing 0.1% FBS for 3 h. Mitochondrial function was evaluated according to the oxygen consumption rate (OCR) using a Seahorse XF Cell Mito Stress Test kit in a Seahorse XFe96 Flux Analyzer (Agilent, Santa Clara, CA). The compounds oligomycin (1 μM), carbonyl cyanide 4-(trifluoromethoxy) phenylhydrazone (FCCP, 2 μM), and a mixture of rotenone and antimycin A (RAA, 1 μM) were serially injected to measure basal OCR, ATP generation, maximal OCR, and spare capacity. For the glycolysis stress test, extracellular acidification rate (ECAR) was measured with the sequential injection of glucose (10 mM), oligomycin (1 μM), and 2-deoxyglucose (50 mM) using a Seahorse XF Glycolysis Stress Test Kit. For the ATP-rate assay, OCR and ECAR were measured with the sequential injection of oligomycin (1 μM) and RAA (1 μM). For the fatty acid oxidation (FAO) assay, RPE cells were starved in DMEM containing 0.5 mM glucose, 1 mM GlutaMAX, 0.5 mM carnitine, and 1% FBS for 6 h. Forty-five minutes prior to the test, RPE cells were cultured in FAO assay media. Just prior to starting

the assay, palmitate-BSA or BSA was added. FAO was measured with the sequential injection of oligomycin (1 μM), FCCP (2 μM), and RAA (1 μM).

Western blot analysis

Western blot analysis was performed as described previously[41]. Cells were lysed in a cell lysis buffer (50 mM Tris–HCl, pH 6.8, containing 10% glycerol, 2% SDS, and 1% proteinase inhibitor cocktail). The cell lysates were shaken at 4 °C for 1 h and centrifugated at 10,000 × g for 10 min. The supernatants were collected for sample preparation. Equal amounts of total cellular proteins (25 μg) were resolved on SDS-PAGE gels and transferred onto nitrocellulose membranes. Membranes were blocked with 10% nonfat milk in Tris-buffered saline with 0.1% Tween-20 (TBST) for 2 h. Membranes were incubated in primary antibodies at 4 °C overnight and secondary antibodies for 2 h. All antibodies were diluted in TBST containing 5% bovine serum albumin (BSA). β-Actin was used as a loading control.

Co-immunoprecipitation (co-IP) assays were performed as described[48]. Briefly, cells were lysed in 150 mM NaCl containing 0.5% NP40 and 1% Triton X-100 (pH 7.5) at 4 °C for 1 h. After centrifugation, the cell supernatant was mixed with anti-c-Myc agarose (#A7470, Sigma, Saint Louis, MO) or anti-Flag M2 affinity gel (#A2220, Sigma). The supernatant and agarose were rotated at 4 °C overnight. After washing by TBST buffer, the samples were loaded for Western blot analysis. Details of primary and secondary antibodies used in this study are shown in Supplementary Table 4.

Immunostaining

Eye sections. Human donor eyes were dissected and preserved in Davidson's fixation solution within 12 h postmortem, followed by paraffin embedding and sectioning (Minnesota Lions Gift of Sight Eyebank, St Paul, MN). Mouse eye paraffin sections were made in-house. Immunohistofluorescence was performed as described[48]. Briefly, sections were deparaffinized and hydrated with xylene, graded ethanol, and distilled water. Antigen retrieval was performed in a steam bath with Tris-EDTA buffer (10 mM Tris base, 1 mM EDTA solution, pH 9.0). Slides were blocked in 5% BSA in PBS containing 0.5% Triton X-100 (PBST) for 2 h. Sections were incubated with primary antibodies for 24 h on a rocking platform at 4 °C. Then, the sections were washed and incubated with secondary antibodies and DAPI for 2 h. The sections were mounted with VECTASHIELD Vibrance antifade mounting medium (Vector Laboratoris, Inc. Burlingame, CA USA). Slides were imaged under an Olympus FV1200 spectral laser scanning confocal microscope (Center Valley, PA). The intensity of immunostaining in retinal sections was quantified using a color histogram in Image J software[49].

Eyecup flatmounts

Following euthanization, mouse eyes were enucleated and collected. The eyes were fixed in 4% PFA in PBS for 30 min. The anterior segment, lens, and retina were removed. The remaining eyecup was flattened by applying four complete radial cuts toward the eyecup center. The eyecup was rinsed in PBS and blocked in 5% BSA in PBST for 2 h. The eyecup flat mount was incubated with primary antibodies at 4 °C overnight. Then, the eyecup was washed and incubated with florescent labeled secondary antibodies for 2 h. The eyecup was mounted on a glass slide with the RPE layer face up using the antifade mounting medium (Vector Laboratoris, Inc. Burlingame, CA).

Retinal flatmounts were imaged with a Cytation 1 imaging reader (Agilent BioTek, Santa Clara, CA). Details of primary and secondary antibodies used in this study are shown in Supplementary Table 4.

Statistics and reproductivity

At least six mice per group were used for the animal experiments. At least three replicates were performed separately for cell culture experiments. All values were presented as mean ± standard deviation (SD). Statistical analyses were performed using GraphPad Prism version 10.1.0 (San Diego, CA)

with a two-tailed Student's *t*-test to compare two groups or a one-way ANOVA followed by the Student–Newman–Keuls test when more than two groups were compared. A *p* value of < 0.05 was considered statistically significant.

Reporting summary

Further information on research design is available in the Nature Portfolio Reporting Summary linked to this article.

Data availability

Data are available in the main article, figures, tables, supplementary materials and in supplementary Excel files. All uncropped and unedited images of Western blotting were included in the supplementary information (Supplementary Fig. 9). Values for all data points in graphs are reported in the separate Excel file named "Supplementary Data 1". The scRNA-seq datasets used in this study have been deposited into the Gene expression Omnibus (GEO) database (accession number GSE221952). All codes for scRNA-seq analysis are available from the corresponding authors upon reasonable request.

References

1. Fleckenstein, M. et al. Age-related macular degeneration. *Nat. Rev. Dis. Prim.* **7**, 31 (2021).
2. Morris, B., Imrie, F., Armbrecht, A. M. & Dhillon, B. Age-related macular degeneration and recent developments: new hope for old eyes? *Postgrad. Med. J.* **83**, 301–307 (2007).
3. Hwang, J. C., Del Priore, L. V., Freund, K. B., Chang, S. & Iranmanesh, R. Development of subretinal fibrosis after anti-VEGF treatment in neovascular age-related macular degeneration. *Ophthalmic Surg. Lasers Imaging* **42**, 6–11 (2011).
4. Daniel, E. et al. Risk of scar in the comparison of age-related macular degeneration treatments trials. *Ophthalmology* **121**, 656–666 (2014).
5. Ambati, J. & Fowler, B. J. Mechanisms of age-related macular degeneration. *Neuron* **75**, 26–39 (2012).
6. Qiang, W., Wei, R., Chen, Y. & Chen, D. Clinical pathological features and current animal models of type 3 macular neovascularization. *Front. Neurosci.* **15**, 734860 (2021).
7. Bazan, N. G. Homeostatic regulation of photoreceptor cell integrity: significance of the potent mediator neuroprotectin D1 biosynthesized from docosahexaenoic acid: the Proctor Lecture. *Investig. Ophthalmol. Vis. Sci.* **48**, 4866–4881 (2007).
8. Zhou, M. et al. Role of epithelial-mesenchymal transition in retinal pigment epithelium dysfunction. *Front. Cell Dev. Biol.* **8**, 501 (2020).
9. Tenbrock, L. et al. Subretinal fibrosis in neovascular age-related macular degeneration: current concepts, therapeutic avenues, and future perspectives. *Cell Tissue Res.* **387**, 361–375 (2022).
10. Somasundaran, S., Constable, I. J., Mellough, C. B. & Carvalho, L. S. Retinal pigment epithelium and age-related macular degeneration: A review of major disease mechanisms. *Clin. Exp. Ophthalmol.* **48**, 1043–1056 (2020).
11. Go, G. W. & Mani, A. Low-density lipoprotein receptor (LDLR) family orchestrates cholesterol homeostasis. *Yale J. Biol. Med.* **85**, 19–28 (2012).
12. Haines, J. L. et al. Functional candidate genes in age-related macular degeneration: significant association with VEGF, VLDLR, and LRP6. *Invest. Ophthalmol. Vis. Sci.* **47**, 329–335 (2006).
13. Chen, Y., Hu, Y., Lu, K., Flannery, J. G. & Ma, J. X. Very low density lipoprotein receptor, a negative regulator of the wnt signaling pathway and choroidal neovascularization. *J. Biol. Chem.* **282**, 34420–34428 (2007).

14. Chen, Y. et al. Photoreceptor degeneration and retinal inflammation induced by very low-density lipoprotein receptor deficiency. *Microvasc. Res.* **78**, 119–127 (2009).

15. Ma, X. et al. Soluble very low-density lipoprotein receptor (sVLDLR) inhibits fibrosis in neovascular age-related macular degeneration. *FASEB J* **35**, e22058 (2021).

16. Chen, Q. et al. Fenofibrate inhibits subretinal fibrosis through suppressing TGF-β-Smad2/3 signaling and Wnt signaling in neovascular age-related macular degeneration. *Front. Pharmacol.* **11**, 580884 (2020).

17. Wang, Z., Liu, C. H., Huang, S. & Chen, J. Wnt Signaling in vascular eye diseases. *Prog. Retin. Eye Res.* **70**, 110–133 (2019).

18. Kim, K. K., Sheppard, D. & Chapman, H. A. TGF-beta1 signaling and tissue fibrosis. *Cold Spring Harb. Perspect. Biol.* **10**, a022293 (2018).

19. Miguel, V. et al. Renal tubule Cpt1a overexpression protects from kidney fibrosis by restoring mitochondrial homeostasis. *J. Clin. Invest.* **131**, e140695 (2021).

20. Schlaepfer, I. R. & Joshi, M. CPT1A-mediated fat oxidation, mechanisms, and therapeutic potential. *Endocrinology* **161**, https://doi.org/10.1210/endocr/bqz046 (2020).

21. Hua, W., Ten Dijke, P., Kostidis, S., Giera, M. & Hornsveld, M. TGFβ-induced metabolic reprogramming during epithelial-to-mesenchymal transition in cancer. *Cell Mol. Life Sci.* **77**, 2103–2123 (2020).

22. Selvarajah, B., Azuelos, I., Anastasiou, D. & Chambers, R. C. Fibrometabolism-an emerging therapeutic frontier in pulmonary fibrosis. *Sci. Signal.* **14**, aay1027 (2021).

23. Wu, Q. et al. ppGalNAc-T4-catalyzed O-Glycosylation of TGF-β type II receptor regulates breast cancer cells metastasis potential. *J. Biol. Chem.* **296**, 100119 (2021).

24. Lee, K. et al. Receptor heterodimerization as a novel mechanism for the regulation of Wnt/beta-catenin signaling. *J. Cell Sci.* **127**, 4857–4869 (2014).

25. Ren, S. et al. LRP-6 is a coreceptor for multiple fibrogenic signaling pathways in pericytes and myofibroblasts that are inhibited by DKK-1. *Proc. Natl Acad. Sci. USA* **110**, 1440–1445 (2013).

26. Singh, H. D., Ma, J. X. & Takahashi, Y. Distinct roles of LRP5 and LRP6 in Wnt signaling regulation in the retina. *Biochem. Biophys. Res. Commun.* **545**, 8–13 (2021).

27. Hata, A. & Chen, Y. G. TGF-β signaling from receptors to Smads. *Cold Spring Harb. Perspect. Biol*. **8**, https://doi.org/10.1101/cshperspect.a022061 (2016).

28. Henderson, J. & O'Reilly, S. The emerging role of metabolism in fibrosis. *Trends Endocrinol. Metab.* **32**, 639–653 (2021).

29. Saika, S. TGFbeta pathobiology in the eye. *Lab. Investig.* **86**, 106–115 (2006).

30. Meyers, E. A. & Kessler, J. A. TGF-beta family signaling in neural and neuronal differentiation, development, and function. *Cold Spring Harb. Perspect. Biol.* **9**, a022244 (2017).

31. Kanow, M. A. et al. Biochemical adaptations of the retina and retinal pigment epithelium support a metabolic ecosystem in the vertebrate eye. *Elife* **6**, e28899 (2017).

32. Schoors, S. et al. Fatty acid carbon is essential for dNTP synthesis in endothelial cells. *Nature* **520**, 192–197 (2015).

33. Joyal, J. S. et al. Corrigendum: Retinal lipid and glucose metabolism dictates angiogenesis through the lipid sensor Ffar1. *Nat. Med.* **22**, 692 (2016).

34. Hewitson, T. D. & Smith, E. R. A metabolic reprogramming of glycolysis and glutamine metabolism is a requisite for renal fibrogenesis-why and how? *Front. Physiol.* **12**, 645857 (2021).

35. Melkonian, E. A. & Schury, M. P. In *StatPearls* (StatPearls Publishing Copyright © 2023, StatPearls Publishing LLC., 2023).

36. Nam, H. et al. The TGF-β/HDAC7 axis suppresses TCA cycle metabolism in renal cancer. *JCI Insight* **6**, e148438 (2021).

37. Wang, Y. et al. Drp1-mediated mitochondrial fission promotes renal fibroblast activation and fibrogenesis. *Cell Death Dis.* **11**, 29 (2020).

38. Park, S. W., Kim, J. H., Park, W. J. & Kim, J. H. Limbal approach-subretinal injection of viral vectors for gene therapy in mice retinal pigment epithelium. *J. Vis. Exp.* **7**, e53030 (2015).

39. Chen, Q., Takahashi, Y., Oka, K. & Ma, J. X. Functional differences of very-low-density lipoprotein receptor splice variants in regulating Wnt signaling. *Mol. Cell Biol.* **36**, 2645–2654 (2016).

40. Hara, M. et al. PNPLA2 mobilizes retinyl esters from retinosomes and promotes the generation of 11-cis-retinal in the visual cycle. *Cell Rep.* **42**, 112091 (2023).

41. Ma, X. et al. ADAM17 mediates ectodomain shedding of the soluble VLDL receptor fragment in the retinal epithelium. *J. Biol. Chem.* **297**, 101185 (2021).

42. Shang, P., Stepicheva, N. A., Hose, S., Zigler, J. S. Jr. & Sinha, D. Primary cell cultures from the mouse retinal pigment epithelium. *J. Vis. Exp.* https://doi.org/10.3791/56997 (2018).

43. Fernandez-Godino, R., Garland, D. L. & Pierce, E. A. Isolation, culture and characterization of primary mouse RPE cells. *Nat. Protoc.* **11**, 1206–1218 (2016).

44. Lehmann, G. L. et al. Single-cell profiling reveals an endothelium-mediated immunomodulatory pathway in the eye choroid. *J. Exp. Med.* **217**. https://doi.org/10.1084/jem.20190730 (2020).

45. Chen, Y. et al. Interleukin-17-mediated protective cytokine signaling against degeneration of the retinal pigment epithelium. *Proc. Natl Acad. Sci. USA* **120**, e2311647120 (2023).

46. Hao, Y. et al. Integrated analysis of multimodal single-cell data. *Cell* **184**, 3573–3587.e3529 (2021).

47. Wu, T. et al. clusterProfiler 4.0: A universal enrichment tool for interpreting omics data. *Innovation* **2**, 100141 (2021).

48. Wu, W. et al. The interplay of environmental luminance and genetics in the retinal dystrophy induced by the dominant RPE65 mutation. *Proc. Natl Acad. Sci. USA* **119**, e2115202119 (2022).

49. Schneider, C. A., Rasband, W. S. & Eliceiri, K. W. NIH Image to ImageJ: 25 years of image analysis. *Nat. Methods* **9**, 671–675 (2012).

Author contributions

X.M., W.W., M.H., C.P., and Y.T. performed the experiments. X.M., J.Z., and Y.T. wrote the R scripts and conducted the data analysis of scRNA-seq datasets. X.M. and W.W. wrote original draft of manuscript. C.M.S., C.T.G., J.C., J.M., and Y.T. designed the research, analyzed data, and wrote and edited the manuscript. J.M. and Y.T. are the guarantors of this work and, as such, have full access to all the data in this study and take responsibility for the integrity of these data and the accuracy of the data analysis.

Competing interests

The authors declare no competing interests.

Additional information

Supplementary information The online version contains supplementary material available at
https://doi.org/10.1038/s42003-024-06773-7.

Correspondence and requests for materials should be addressed to Jian-Xing Ma or Yusuke Takahashi.

Peer review information *Communications Biology* thanks James Hurley and the other, anonymous, reviewer(s) for their contribution to the peer review of this work. Primary Handling Editor: Joao Valente. A peer review file is available.

Reprints and permissions information is available at
http://www.nature.com/reprints

Publisher's note Springer Nature remains neutral with regard to jurisdictional claims in published maps and institutional affiliations.